Title
Experimental and Modeling Study of Methane Adsorption onto Partially Saturated Shales

Journal
Water Resources Research, 54(7)

ISSN
0043-1397

Authors
Wang, Lu
Wan, Jiamin
Tokunaga, Tetsu K
et al.

Publication Date
2018-07-01

DOI
10.1029/2017wr020826

Peer reviewed

Experimental and Modeling Study of Methane Adsorption onto Partially Saturated Shales

Lu Wang[1,2], Jiamin Wan[2], Tetsu K. Tokunaga[2], Yongman Kim[2], and Qingchun Yu[1]

[1] School of Water Resources and Environment, China University of Geosciences (Beijing), Beijing, China, [2] Energy Geosciences Division, Lawrence Berkeley National Laboratory, Berkeley, CA, USA

Correspondence to: Q. Yu, yuqch@cugb.edu.cn

Abstract

Shale gas equilibrates through gas-liquid-solid interactions in reservoirs, but the role of moisture is rarely investigated. To determine how adsorbed water influences methane behavior, three carboniferous shale samples from the Qaidam Basin, China, were humidified at five levels up to a relative humidity of 89%, and their methane capacities at pressures up to 12 MPa were studied. The experimental results indicate that two water-related mechanisms, “water blocking for methane transport” and “surface competition for gas-solid interaction,” are primarily responsible for the methane capacity variations. A compositional comparison suggests that a high abundance of clay minerals plays a favorable role in methane migration by retaining water in interlayer pores. Based on the experimental data, an optimized method for calculating the adsorption amount based on an approximation of density distribution is proposed. The model predicts the average thickness of the adsorption layer and the adsorbed methane density distribution on the surface at a given pressure. The methane adsorption layer “thins” in a stepped pattern by up to 45% in the presence of water, with little further change observed at relative humidities greater than 75% in the studied samples.

1 Introduction

Shale gas has become one of the most important energy resources in recent years because of advances in well drilling and stimulation technologies, which have led to large amounts of natural gas production from shales. Gas predominantly occurs as free gas in pores and fractures, as adsorbed gas on the surface of organic matter and inorganic components and as a small amount of dissolved gas in water, oil, and bitumen (Guo et al., 2014). The adsorption capacity is an important parameter that has been widely reported (Chalmers & Bustin, 2008; Chen et al., 2011; Heller & Zoback, 2014; Ross & Bustin, 2007a; Weniger et al., 2010; Zhang et al., 2012), but the dependence of the adsorption isotherms on the pressure and moisture is worthy of further analysis.

Moisture content is an important component of the gas shale reservoir system as the amount and distribution of water can have adverse effects on the volume of adsorbed and free gas, as well as on the relative permeability/

diffusivity. Most shales contain a certain amount of water, which stably interacts with the pore surfaces and presents a difficulty in removal below 313.15 K (Heller & Zoback, 2014). Tokunaga et al. (2017) conducted water adsorption studies on crushed shale and observed significant saturation hysteresis. Their results quantified the severity of the water blocking problem and suggested that gas production from unconventional reservoirs is largely associated with stimulated regions that have had little or no exposure to injected water. With respect to the adsorption, although many studies have stressed the impact of moisture on methane adsorption in coal (Busch et al., 2004; Clarkson & Bustin, 2000; Fitzgerald et al., 2005; Ji et al., 2012), the issue of how moisture in inorganic-dominated shales influences the methane-surface interaction is under debate. Conventional wisdom suggests that water molecules reduce the sorption sites for gas, which contributes to a reduction of the methane capacity (Joubert et al., 1974; Levy et al., 1997). Controversially, several authors have suggested that moisture acts as a diluent for gas sorption (Yee et al., 1993). Hatch et al. (2012) determined the water adsorption capabilities of kaolinite, illite, and montmorillonite clays at room temperature (298 K) using horizontal attenuated total reflectance and Fourier transform infrared spectroscopy with a flow cell. They investigated submonolayer water adsorption up to monolayer coverage at a relative humidity (RH) of 13%, which was followed by mesopores (13–76% RH) and finally multilayer water adsorption (76% RH). Density functional theory (DFT) and grand canonical Monte Carlo methods have been successfully applied to describe adsorption of supercritical gases with simple molecular structures, such as methane, argon, and carbon dioxide, onto geometrically simple surfaces. Jin and Firoozabadi (2014) performed a series of grand canonical Monte Carlo simulations on clay and suggested that in micropores, water, carbon dioxide, and methane adsorb within the same layer; water molecules adsorb onto the first layer, and CO_2 and methane exhibit a weak second-layer adsorption in mesopores and macropores. Unfortunately, the complexity of the pore system in shales precludes using the conclusions from an ideal geometric surface to explain the effect of moisture on the methane capacity of shales. Moreover, few studies have investigated the methane capacity of partially saturated shales.

High-pressure methane isotherms exhibit an “adsorption maximum,” and substantial effort has been devoted to obtaining a reasonable explanation for this behavior (Zhou et al., 2000). Zheng and Gu (1998) predicted the isotherms of CO–CO_2 mixtures and CO_2–N_2 mixtures on Cu (I) –NaY zeolite using a modified van der Waals equation of state (EOS). The authors compared their model to extensively published models confirming that the semiempirical EOS of the authors' model is in better agreement with experimental data than traditional gas-liquid EOSs for gas-solid interactions. Their results provide a new calculation insight in dealing with the “adsorption maximum” observed in extensive experiments. Murata and Kaneko (2000)

proposed an iteration procedure to obtain the Gibbs adsorption amount and applied it to the high-pressure CH_4 adsorption capacity determination on nonporous carbon black and microporous carbon from 273 to 303 K. With a consideration of the adsorbed gases, their new data processing can effectively avoid the adsorption maximum phenomenon and increase the adsorption amount to ~3 times or more. Reports in the literature have proposed extensive improvements to Gibbs data processing, as the current methods involve complex models based on different theoretical assumptions, with little direct data application.

Our objective in this paper was to experimentally analyze methane behavior in shales with different moisture contents and predict the adsorption amount using an optimized model. The effect of water on methane adsorption varies with the compositional/structural characteristics. By analyzing the experimental and modeling results, we determined the pores and pressure zone in which water significantly affects methane transport and adsorption.

2 Experiments

2.1 Samples

The investigated shale samples were from core extracted from the Carboniferous Keluke Group Formation in the eastern Qaidam Basin, China. Three samples were chosen from the Chaiye-2 core-drilling well in the Shihuigou region at depths of 938.5, 966.5, and 1,048.2 m considering the sufficiency of the sample supply. Geochemical methods were used to characterize the composition and structure of the samples to provide references for the methane capacity comparison. The geochemical tests were performed using several methods (Wang & Yu, 2016). A carbon sulfur analyzer was used to determine the total organic carbon (TOC) content, and the determination was provided by North China Petroleum Analysis Lab, Renqiu, China. A quantitative mineralogical analysis was conducted using the X-ray diffraction method by the Micro Structure Analyzing and Testing Lab, Beijing, China. A microscope (equipped with F7000 MPV-SP, Hitachi, Japan) was used to determine the vitrinite reflectance, which represents the maturity of the organic matter.

Several methods were used to characterize different ranges of pore volume and surface areas, and the determination was provided by Beijing Center for Physical and Chemical Analysis, Beijing, China. The macropore size distribution was measured using mercury intrusion porosimetry (MIP, Pore Master GT 60, Quantachrome, from 0.8 to 30,000 psi). The low-pressure N_2-adsorption isotherm was measured at a temperature of 78 K and a pressure below 1.27 bar. The sorption curve was analyzed for volume estimation using Barrette-Joynere-Halenda and DFT methods, and for surface area estimation using the Brunaue-Emmet-Teller equation (Groen et al., 2003). Low-pressure CO_2 adsorption experiments were conducted at relative pressures of 0–0.03 and absolute pressures of 0–1.15 bar at 273 K (Li et al., 2015). The DFT

method was applied in calculating the micropore volume and surface area distribution from the adsorption isotherm curve.

2.2 Methane Adsorption

In the moisture studies, approximately 15 g of the shale was weighed to an accuracy of 0.001 g and then sealed for a week in a desiccator at 313 K to remove ambient moisture. For the adsorption measurements on dry samples, the samples were vacuum dried in the apparatus at 313 K for an additional 9 to 12 hr.

Moisture equilibration of the samples was performed at 313.15 K with saturated aqueous salt solutions to keep the RH at selected values from 22 to 89% (Greenspan, 1977). The salts (VWR Co., USA), and their associated RH are presented in Table 1. The crushed sample (<200 mesh, 0.074 mm) was evenly spread as a thin layer in a 6 cm × 6 cm aluminum plate suspended above the selected saturated salt solution in a sealed desiccator. The moisturizing procedure was conducted for at least one week (reaching constant sample mass), after which the shale was transferred to the sample cell.

Table 1

Relative Humidities Controlled by Various Aqueous Salt Solutions (Greenspan, 1977)

	$CaCl_2$[a]	$Mg(NO_3)_2$[b]	NaCl[b]	KBr[b]	KNO_3[b]
RH (%)	22	48	75	79	89

[a]The relative humidity refers to the data provided by the calcium chloride handbook from Dow Company, New York, USA. [b]The relative humidity refers to the data provided by Greenspan (1977) at a temperature of 313.15 K.

The methane adsorption experiments were conducted using a static manometric method (Merkel, Gensterblum, et al., 2015; Wang & Yu, 2016). For samples of S_#1 and S_#2, the experiments were conducted at Lawrence Berkeley National Laboratory, Berkeley, California, USA. As shown in Figure 1, the experimental setup consisted of three main components: a gas inlet system, an adsorption system, and a monitoring system. The gas inlet system involved high-pressure methane with a purity of 99.99%, which was provided by Praxair Inc., USA, and a 500D syringe pump from Teledyne Company, USA. The core of the system included two stainless steel cells, each with a flange sealing shell. The interior volumes of the two cells were calibrated by helium expansion to be 33.73 cm^3 for the reservoir cell (A_1) and 26.96 cm^3 for the sample cell (A_2). All components were placed in a Heratherm incubator (Thermo Scientific, USA) that maintained the temperature to within ±0.2 °C. The monitoring system consisted of an Agilent 34970A data acquisition/switch unit (Agilent Company, USA) that received voltage signals from pressure transducers inserted into the cells through the top shells; the relative error of the pressure measurements was ±0.5%. As to sample S_#3, the methane adsorption experiments were conducted at the China University of Geoscience, Beijing, China. The experimental equipment was introduced by Wang and Yu (2016). The

pressure and temperature sensors of these two laboratories hold the same precision, and they were calibrated with the same standard procedure.

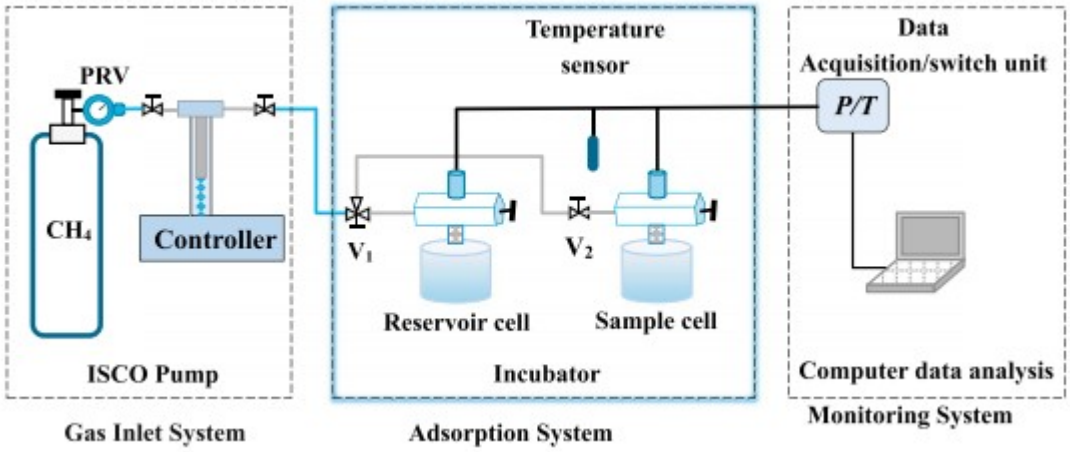

Figure 1

Schematic of the experimental apparatus.

Before methane loading, A_1 and A_2 were vacuum-pumped to remove impurities, and the removal of adsorbed water from the pore system required higher temperatures (Heller & Zoback, 2014). The amount of Gibbs adsorption that corresponds to the first adsorption balance pressure is described as follows:

$$n_1 = \frac{1}{R}\left(\frac{P_r V_r}{T_r Z_r} - \frac{P_r' V_r}{T_r' Z_r'} - \frac{P_s' V_{\text{void}}}{T_s' Z_s'}\right) \quad (1)$$

where n_1 is the adsorbed amount of methane (mol) at the first pressure increase and V_r and V_{void} are the volumes (cm^3) for bulk gas in the reservoir and sample cells, respectively. In this study, V_{void} was obtained by porosity data from the MIP + CO_2 determination to avoid possible moisture loss during the helium expansion (Rexer et al., 2014). P_r and T_r denote the pressure (MPa) and temperature (K) in the reservoir cell before the adsorption, and Z_r denotes the corresponding compressibility factor. When the system reached an adsorption equilibrium after ~6–12 hr, the pressures and temperatures in the reservoir and sample cell were determined and are denoted by P'_r, P'_s, T'_r, and T'_s, respectively. The corresponding compressibility factors are denoted by Z'_r and Z'_s. In equations 1 and 2, R is the universal gas constant.

$$\Delta n = \frac{1}{R}\left(\frac{P_{r,N} V_r}{T_{r,N} Z_{r,N}} - \frac{P_{r,N}' V_r}{T_{r,N}' Z_{r,N}'} + \frac{P_{s,N} V_{\text{void}}}{T_{s,N} Z_{s,N}} - \frac{P_{s,N}' V_{\text{void}}}{T_{s,N}' Z_{s,N}'}\right) \quad (2)$$

In equation 2, Δn is the amount of Gibbs adsorption for one pressure step and $P_{r,N}$ and $P'_{r,N}$ represent the pressures before and after the N_{th} adsorption in the reservoir cell, respectively; the corresponding compressibility factors are denoted by $Z_{r,N}$ and $Z'_{r,N}$. $P_{s,N}$ and $P'_{s,N}$ represent the pressures before and

after the N_{th} adsorption in the sample cell, respectively, and the corresponding compressibility factors are denoted by $Z_{s,N}$ and $Z'_{s,N}$. The first data point was obtained from equation 1, and the subsequent data points were calculated using equation 2. In this study, Z was calculated using the modified Benedict-Webb-Rubin EOS recommended by the National Institute of Standards and Technology (Heller & Zoback, 2014).

According to equations 1 and 2, the amount of accumulating gas (n_N) that corresponds to the N_{th} adsorption balance pressure $P'_{s,N}$ is $n_N = n_1 + \sum_{i=2}^{N} \Delta n_i$, and the amount adsorbed per unit mass of sample is $Q_n = n_N/m_s$, where m_s is the mass of the sample (Li et al., 2015).

3 Modeling

3.1 Density Distribution Configuration

Several models have been used to describe gas sorption on unified porous materials and have been extended to applications involving complicated porous materials such as coal and shales (Clarkson & Bustin, 2000; Yuan et al., 2014). These models are derived from different theoretical bases to mainly estimate the adsorption capacity, with less investigations on the physical significance of the related parameters. However, some parameters can reveal useful information about the adsorption mechanism, which was explored using the analytical model established in our work.

The optimized model proposed in this study considers the density distribution of methane adjacent to the shale surface. The model is based on the assumption that the density can be approximated by a normal distribution curve, which resembles the estimation of the change in density with the gas-solid interactions given by the Monte Carlo calculations of Titiloye and Skipper (2000). Other fitting curves, such as those involving polymers and S-functions, would produce weaker correlation coefficients than the normal distribution after several tries.

In Figure 2, the blue curve represents the methane density ρ as a function of the distance $r$from the surface. The Gibbs adsorption amount, which is also known as the amount of excess surface adsorption, can be represented by the area of region S_1, and the absolute gas adsorption amount is expressed as the area of $S_1 + S_2$. In the simulation of Ambrose et al. (2010), the density of the first adsorption layer (closest to the wall, i.e., ρ_1) ranges from 0.48 to 0.57 g/cm^3 for pores from 3.6 to 1.95 nm. In this study, 0.57 g/cm^3 is used to approximate the density of the first adsorption layer based on the consideration of the major pore size of our shale samples. The parameter r_1 represents the average distance of the first adsorption layer from the shale surface, and r_1 = 0.4 nm is used as simulations indicate that methane molecules remain approximately 0.38–0.4 nm from a simulated surface (Mosher et al., 2013; Titiloye & Skipper, 2000). The density of the

bulk gas at a given pressure is represented as ρ_2, and r_2 is the thickness of the adsorption layer.

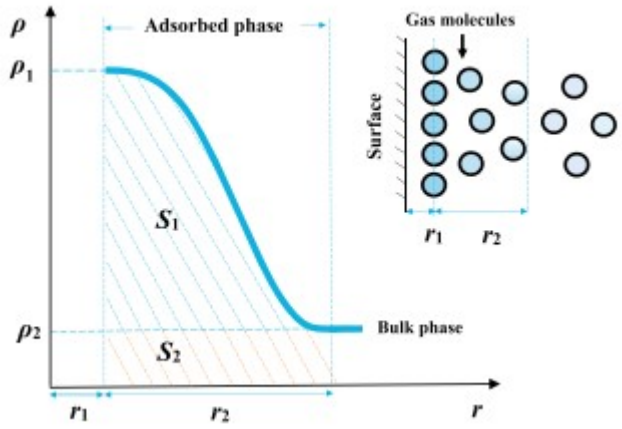

Figure 2

Interpretation of the methane density distribution in the adsorption state.

3.2 Absolute Adsorption Model

The framework of the function is expressed as

$$y = \frac{1}{\sigma\sqrt{2\pi}} \exp\left(-\frac{(x-\mu)^2}{2\sigma^2}\right) \quad (3)$$

where μ and σ are the mean and variance of the normal distribution, respectively. Because equation 3 is applied to approximate the methane density distribution at the surface, both $\mu$and σ have physical meanings. The parameter μ represents the distance between the adsorbent surface and the first adsorption layer of methane (equivalent to r_1 in Figure 2), which is assumed to be 0.4 nm as discussed previously, and σ relates to the density at a given gas-solid distance; a larger σ indicates a “flatter and wider” density distribution. When water is present, its strong dipole results in a strong affinity to clay surfaces, whereas methane is supplanted and unable to form the same multiple layers. The weaker gas-liquid interactions can be reflected by the parameter σ.

Following the configuration in Figure 2, an adsorbed methane density of ρ (y in equation 3) depends on the gas-surface distance r (x in equation 3). Therefore, we can derive equations 4 and 5 from equation 3:

$$\rho = a\frac{1}{\sigma\sqrt{2\pi}} \exp\left(-\frac{\left(r-0.4\times10^{-7}\right)^2}{2\sigma^2}\right) \quad (4)$$

$$a = 0.57\sigma\sqrt{2\pi} \quad (5)$$

where r is the gas-solid distance in cm, ρ is the density of methane in g/cm^3, and a is an intermedia parameter that is used to keep the maximum of ρ free from σ. The adsorption layer thickness (ALT), which is shown as r_2 in Figure 2,

can be obtained using equations 4 and 5) if σ is also known. However, σ cannot be calculated directly, so we treated it as an optimization parameter in the following calculation.

The amount of bulk gas in the adsorbed phase (S_2 in Figure 2) is calculated as

$$n_{bulk} = Sr\rho_{bulk} \quad (6)$$

where ρ_{bulk} is the density of the bulk methane, n_{bulk} is the amount of gas in the adsorbed phase with bulk density, and S represents the surface area of the pores that are effective for methane (0.7–7 nm; Kowalczyk et al., 2005; Liu et al., 2016; Rexer et al., 2014; Yang et al., 2010). For a known surface area and density distribution, the absolute adsorption amount can be calculated by equation 7:

$$n_{ab} = S\int_{r_1}^{r_2}\rho \mathrm{d}r = Sa\frac{1}{\sigma\sqrt{2\pi}}\int_{-\infty}^{r_2}\exp\left(-\frac{\left(r-0.4\times10^{-7}\right)^2}{2\sigma^2}\right)dr - 0.5a \quad (7)$$

where n_{ab} is the absolute adsorption amount. The value of σ can be calculated using an optimization process. The objective function is defined using equations 8 to 10:

$$n_{Gibbs} = n_{ab} - n_{bulk} = n_{ab} - Sr\rho_{bulk} \quad (8)$$

$$\Delta n' = n_{Gibbs\_cal} - n_{Gibbs\_exp} \quad (9)$$

$$J = \frac{1}{N}\sum_{i=1}^{N}\frac{\Delta n'}{n_{Gibbs\_exp}} \quad (10)$$

where $\Delta n'$ is the difference between calculated (n_{Gibbs_cal}) and experimental data (n_{Gibbs_exp}). The function J in equation 10 is used to demonstrate the deviation between the predicted and experimental data. The minimum value of J corresponds to the target Gibbs adsorption amount with σ and a calculated. This process was performed iteratively based on the interior-reflective Newton method (Coleman & Li, 1996).

4 Results and Discussion

4.1 Shale Characterization

Shale samples from the Chaiye-2 drilling well (including samples for this study) have been introduced in our former research (Wang & Yu, 2016).

The TOC values from a carbon/sulfur analyzer for S_#1 – S_#3 are 1.67%, 2.88%, and 1.67%. The vitrinite reflectance values obtained by rock pyrolysis indicate a higher maturity of the kerogen in S_#2 (1.59% R_0) relative to S_#1 and S_#3 (1.49% and 1.13% R_0). Both S_#1 and S_#2 have reached the gas window, and they belong to the condensate and moisture zones, where gas is mainly generated by thermal cracking (Zhang et al., 2014).

The CH_4 sorption capacity varies significantly among different clay types. Ji et al. (2012) used experiments to show that montmorillonite-based bentonite

has a much larger CH_4 sorption capacity than illite/smectite interstratified clay (I–S mixed-layer clay) or kaolinite. For samples of S_#1 to S_#3, the illite/smectite interstratified clay made up the dominant proportion at 53%, 55%, and 58%, followed by the kaolinite (22%, 29%, and 25%) and the illite (15%, 8%, and 26%).

The pore surface area distributions are plotted in Figures 3-5. Micropores are the greatest contributor to the surface area, and the CO_2 determined micropore surface area of S_#2 (18.035 m^2/g) is larger than that of S_#1 and S_#3 (12.446 and 10.330 m^2/g). A distinctive proportion of surface area concentrates in pores of 0.4–0.8 nm in S_#1, which account for 73% of the total micropore surface area (0.3–2 nm). The surface area in both S_#2 and S_#3 is distributed in smaller pores (0.3–0.6 nm), which account for ~70% of the total micropore surface area.

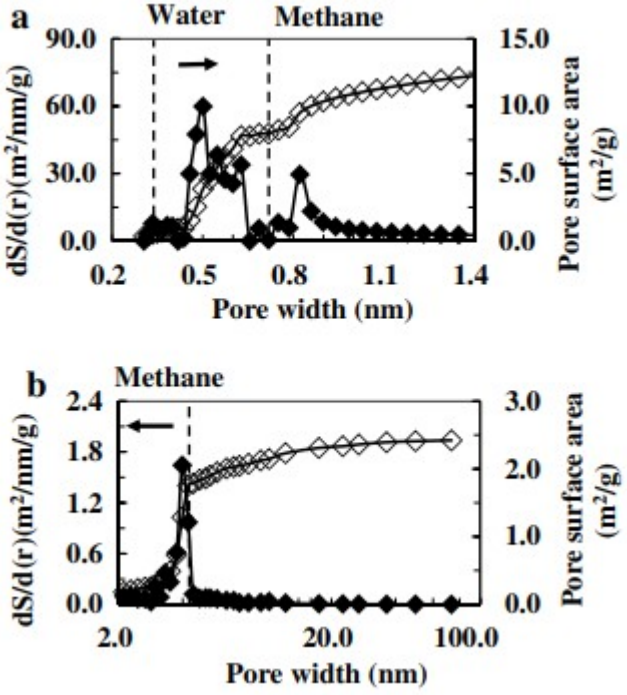

Figure 3

Pore surface area distributions of S_#1 determined by (a) CO_2 and (b) N_2 adsorption. The solid diamonds indicate the divided surface area at a given pore width, with the values and units shown on the left axes, whereas the empty diamonds indicate the cumulative surface area along with the pore width, with the values and units shown on the right axes. The arrows with water and methane on top mark the effective pore ranges for water and methane molecules.

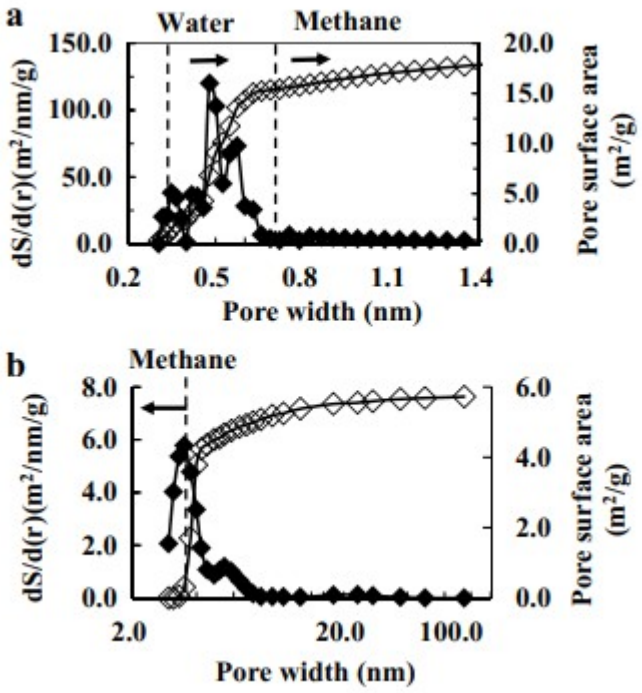

Figure 4

Pore surface area distributions of S_#2 determined by (a) CO_2 and (b) N_2 adsorption. The solid diamonds indicate the divided surface area at a given pore width, with the values and units shown on the left axes, whereas the empty diamonds indicate the cumulative surface area along with the pore width, with the values and units shown on the right axes. The arrows with water and methane on top mark the effective pore ranges for water and methane molecules.

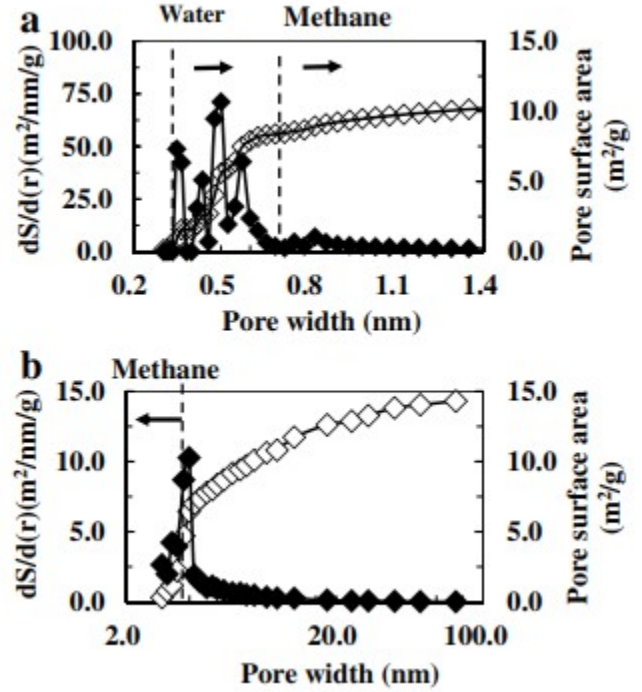

Figure 5

Pore surface area distributions of S_#3 determined by (a) CO_2 and (b) N_2 adsorption. The solid diamonds indicate the divided surface area at a given pore width, with the values and units shown on the left axes, whereas the empty diamonds indicate the cumulative surface area along with the pore width, with the values and units shown on the right axes. The arrows with water and methane on top mark the effective pore ranges for water and methane molecules.

4.2 Adsorption Isotherm of Methane With Different Moisture Contents

As shown in Figure 6, the water adsorption isotherms exhibit faster increases at RH > 48%. Hatch et al. (2012) determined the water adsorption on clays and suggested that at an increased RH of approximately >15–20%, water adsorbs at a faster rate, as monolayers tend to transfer to multiple layers, even exhibiting capillary condensation in major pores. Li et al. (2016) also proposed that when the coverage of water on the solid surface is more than a monolayer, a transition from gas-solid interface interaction to gas-liquid interface adsorption occurs. However, when the coverage is less than a monolayer, strong competition between water and methane molecules for adsorption sites should be considered. In addition to its effect on methane behavior, water influences both the bulk volume and the total weight of the shale (Chenevert, 1970):

$$\rho_{\text{moisture}} = \frac{\rho_{\text{dry}}}{1 + \left(\rho_{\text{dry}} - 1\right) \times \omega} \quad (11)$$

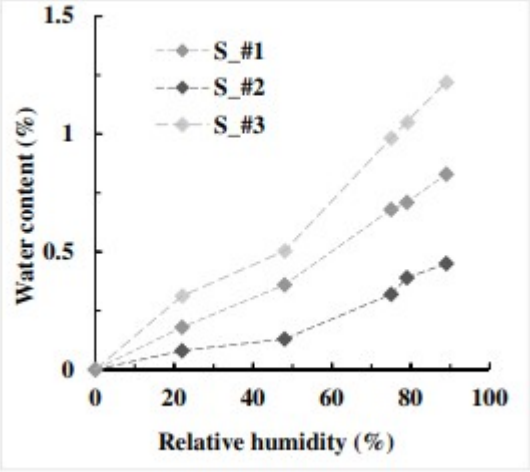

Figure 6

Water adsorption isotherms of the shale samples at 313.15 K.

where ρ_{dry} and ρ_{moisture} represent the densities of dry and moist shales in g/cm^3, respectively, and ω represents the water mass per solid mass. Equation 11 shows that water decreases the shale density, which would contribute to a smaller void volume because $V_{\text{void}} = V_{\text{sample\_cell}} - m_s/\rho_s$, where ρ_s is the shale density in g/cm^3. The water content and the corresponding shale density variation are listed in Table 2.

Table 2
Moisture Content, ω (%), and Shale Density, ρ_s (g/cm^3), With Variations in Relative Humidity

Item	S_#1				
RH (%)	22	48	75	79	89
ω (%)	0.18	0.36	0.68	0.72	0.82
ρ_s (g/cm^3)	2.79	2.79	2.77	2.76	2.76
Item	S_#2				
RH (%)	22	48	75	79	89
ω (%)	0.08	0.13	0.32	0.39	0.45
ρ_s (g/cm^3)	2.70	2.70	2.70	2.69	2.69
Item	S_#3				
RH (%)	22	48	75	79	89
ω (%)	0.31	0.50	0.98	1.05	1.22
ρ_s (g/cm^3)	2.70	2.70	2.69	2.67	2.65

The Langmuir equation is used to predict the absolute adsorption amount at a given pressure (n_{ab}). Unlike the optimized model, it is based on the "monomolecular" layer concept, which is commonly used in practice due to its simplicity and clear physical meaning of fitting parameters. In addition, the Langmuir equation can provide a good representation of the measured sorption data for coals (Crosdale et al., 2008), clays (Hartman et al., 2008; Ji et al., 2012), and even shales (Liu et al., 2016) in both dry and moist conditions (Li et al., 2016).

$$n_{ab} = n_{\max} \frac{K(T)P}{1 + K(T)P} \quad (12)$$

where $n_{\max}$ is the maximum adsorption amount for methane and K (T) is the temperature-dependent parameter. Figures 7–9-7–9 present the experimental and modeling results for methane adsorption onto partially saturated samples up to 12 MPa, and the model shows that the methane capacity decreases by 13–42% at the highest moisture content. Compared to S_#2, the methane capacity of both S_#1 and S_#3 exhibits a moderate decrease in the presence of water. Although numerous studies state that under moist conditions, moisture may render many microporous sorption sites unavailable to CH_4 by filling pore throats or occupying sorption sites (Joubert et al., 1974; Krooss et al., 2002; Ross & Bustin, 2007b), a slight upward trend in the adsorption amount is observed in S_#2 at ω = 0.08% and S_#3 at ω < 0.5% when the pressure is higher than ~6 MPa. Distinct and consistent decreases in capacity occur at 0.18% ≤ ω ≤ 0.68% for S_#1, 0.08% ≤ ω ≤ 0.32% for S_#2, and 0.50% ≤ ω ≤ 1.05% for S_#3. S_#3 exhibits the slowest downward trend and lower adsorption amount as a whole. With increasing moisture content, according to Li et al. (2016), an approximately 0.4-nm-thick layer of adsorbed water forms at RH = 0.7, and the thickness of the layer increases rapidly as RH is increased to 1, which indicates multilayer adsorption transitioning to capillary condensation. On the other hand, Joubert et al. (1974) found that only adsorbed water affects methane adsorption. These results are consistent with our observation that

at RH levels greater than 75% (ω = 0.68% for S_#1, ω = 0.32% for S_#2, and ω = 0.98% for S_#3), water has a minimal influence on methane adsorption.

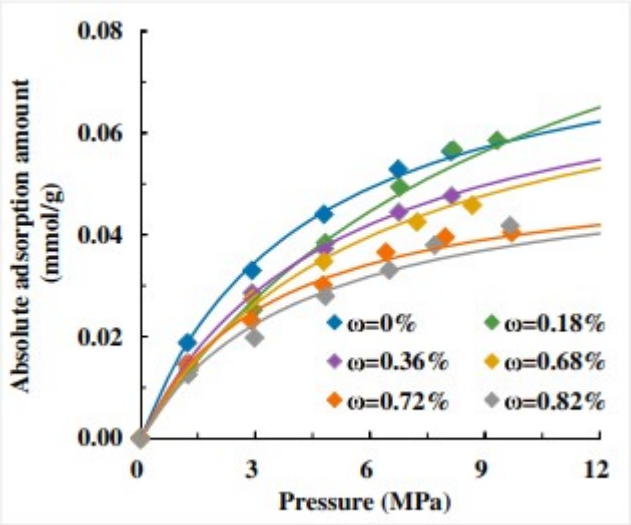

Figure 7

Langmuir isotherms for the methane adsorption of partially saturated S_#1.

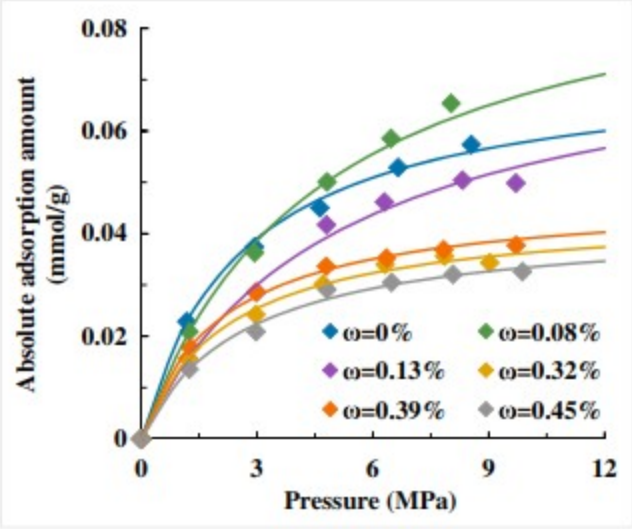

Figure 8

Langmuir isotherms for the methane adsorption of partially saturated S_#2.

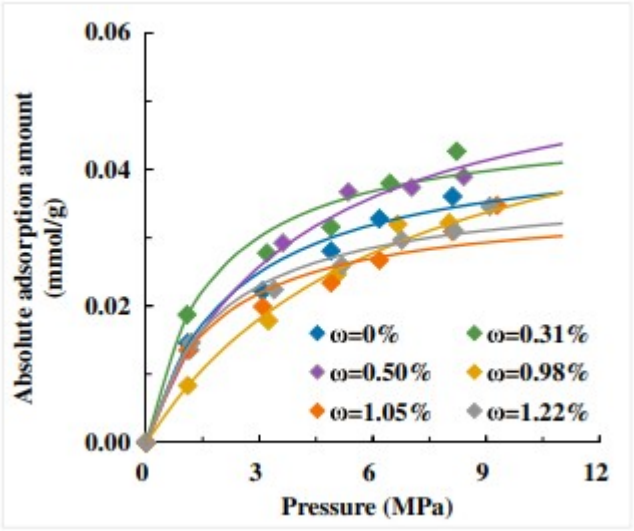

Figure 9

Langmuir isotherms for the methane adsorption of partially saturated S_#3.

Kang et al. (2011) proposed two conceptual models of shale gas transportation. The authors suggested that methane undergoes viscous flow in the inorganic matrix, where water may block the path for methane and where the influence depends on the matrix structure. Tokunaga et al. (2017) proposed that low relative permeabilities also limit the rates of water redistribution within matrix pores, thus allowing the persistence of water blocks at fracture-matrix boundaries. Within the kerogen surrounded by inorganic matter, the state of gas adsorption + diffusion dominates, where water adsorbed on the surface weakens the gas-surface interaction. Their configuration suggests that both the effective sites and the accessible approaches to these sites are influenced by moisture, and the type of moisture influence depends on the sample component and the corresponding structure.

S_#2 has a nearly twofold higher TOC content than S_#1 and S_#3 as well as superior methane capacity under dry conditions. However, S_#2 also has a quartz content of 49%, and lower clay minerals account for 6%, indicating poor access for methane in the presence of water. S_#1 and S_#3 possess higher clay contents of 21% and 46%. With a higher proportion of hydrophilic sites, both the samples possess higher water content and limited methane capacity reduction. This is possibly because the structure benefits methane transportation in the presence of water, as clay tends to retain water compared to quartz.

The regression parameters obtained from the modeling optimizations, including the ALT (r_2), the density distribution σ, the maximum adsorption amount n_{max}, the temperature-dependent parameter K (T), and the correlation coefficient R of the Langmuir fitting, are shown in Table 3. The average value of R from the linearized Langmuir equation is 0.993. The

values of σ also decrease by up to approximately 17%–43%, indicating a "narrow adsorption zone" off the moisture surface. The pore accessibility, the relationship between organic matter and clay minerals, and the blockage and availability of sorption sites must be considered, and further research is required to differentiate these factors (Merkel, Fink, et al., 2015).

Table 3
Parameters of the Optimized Model

Sample	RH (%)	r_2 (nm)	σ (10^{-8}) cm	a (10^{-8}) g/cm^3 × cm	R	n_{max} (mmol/g)	$K(T)$
S_#1	0	0.602	2.982	3.147	0.999	0.085	0.23
	22	0.606	3.123	3.296	0.998	0.120	0.10
	48	0.506	2.521	2.660	0.999	0.079	0.19
	75	0.480	2.568	2.568	0.999	0.080	0.16
	79	0.424	2.090	2.206	0.995	0.054	0.29
	89	0.429	2.235	2.359	0.989	0.055	0.23
S_#2	0	0.481	2.426	2.560	0.998	0.073	0.38
	22	0.556	2.755	2.907	0.998	0.099	0.21
	48	0.426	2.128	2.246	0.998	0.080	0.20
	75	0.285	1.456	1.536	0.997	0.044	0.45
	79	0.308	1.609	1.698	0.998	0.047	0.48
	89	0.265	1.393	1.470	0.994	0.042	0.38
S_#3	0	0.233	1.206	1.273	0.979	0.044	0.43
	22	0.256	1.323	1.396	0.972	0.047	0.58
	48	0.226	1.173	1.238	0.998	0.059	0.26
	75	0.195	1.006	1.062	0.998	0.059	0.15
	79	0.196	1.011	1.067	0.972	0.035	0.54
	89	0.195	1.006	1.062	0.988	0.038	0.52

Note. The adsorbed layer thickness is r_2 (nm), the density distribution parameter is σ (× 10^{-8} cm), the intermedia parameter is a (× 10^{-8} cm), the correlation coefficient of the Langmuir fitting is R, the maximum adsorption amount is n_{max} (mmol/g), and the temperature-dependent parameter, $K(T)$, is up to approximately 9 MPa.

Figures 10-12 indicate that water affects the methane behavior differently with changing pressure. The adsorption amount decreases slightly at 1 MPa by 0.006 mmol/g for S_#1, 0.009 mmol/g for S_#2, and 0.001 mmol/g for S_#3, which has the highest water loading (ω = 0.82% for S_#1, ω = 0.45% for S_#2, and 1.22% for S_#3). The reduction grows to 0.012–0.017 mmol/g for S_#1 and 0.017–0.022 mmol/g for S_#2 at 3–6 MPa. The decreasing trend is slower in S_#3 (~0.003 mmol/g). At a pressure of 9 MPa, the adsorption amount decreases by 0.020 mmol/g in S_#1, 0.024 mmol/g in S_#2, and 0.004 mmol/g in S_#3. The comparison shows that methane capacity is more evidently influenced at pressures of about 3–6 MPa.

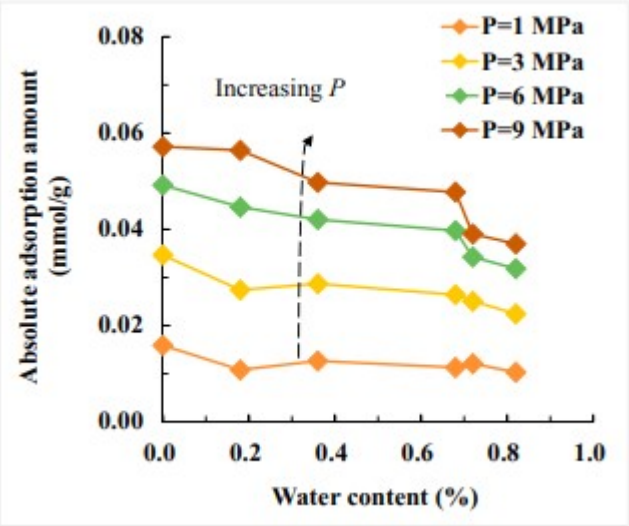

Figure 10

Modeling results of the adsorbed methane amount for various moisture contents and pressures for S_#1. The solid diamonds are the modeling results, and the solid lines are used to illustrate the trends.

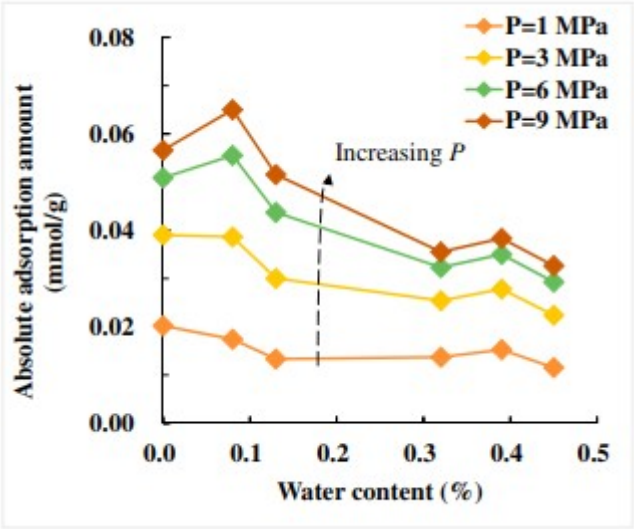

Figure 11

Modeling results of the amounts of adsorbed methane for various moisture contents and pressures for S_#2. The solid diamonds are the modeling results, and the solid lines are used to illustrate the trends.

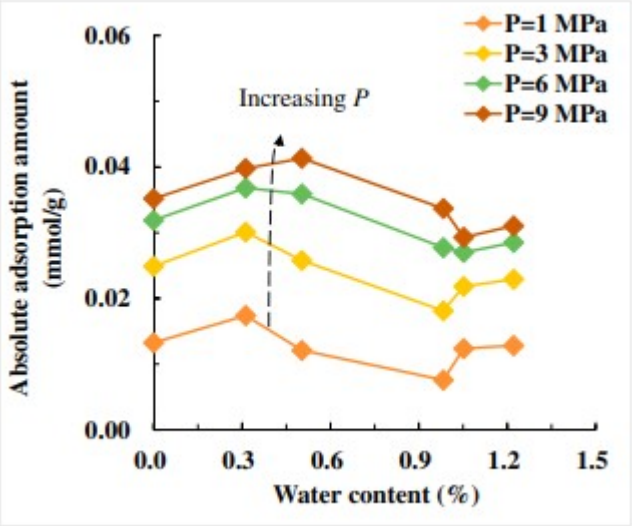

Figure 12

Modeling results of the amounts of adsorbed methane for various moisture contents and pressures for S_#3. The solid diamonds are the modeling results, and the solid lines are used to illustrate the trends.

Organic matter in shales provides the dominant effective sites for methane initially. With accumulated gases, these effective sites tend to saturate, and the proportion of methane on inorganic pore surfaces increases. Although clays facilitate methane adsorption, their sites are strongly influenced by moisture. Water is reported to hinder methane adsorption, leading to a substantially lower adsorbed methane density because of the weaker solid-gas interaction (Jin & Firoozabadi, 2014). At higher pressures caused by the accumulation of hydrocarbons such as methane, the ratio of water in the gas phase will decrease, and water will evaporate into gas phase (Li et al., 2016). Moreover, the adsorption process is more sensitive to the state of the bulk phase at higher pressures. Both factors explain why methane adsorption ceases to decrease evidently at and above 9 MPa. Notably, as the Gibbs data were analyzed with the optimized model and then the Langmuir equation to make the comparison, the modeling results may have fluctuated somewhat compared with the Gibbs data while still showing an accordant trend.

As shown in Figures 10-12, methane adsorption is not strongly influenced at the lowest moisture contents. Regardless of the component, pores with smaller diameters may preferentially hold water, but some of them are limited to methane for its larger dynamic diameter (Liu et al., 2016). In different shales, the distribution of hydrophobic and hydrophilic sorption sites throughout the pore network plays a major role in the effect that moisture has on the methane capacity with regard to blocking pore throats. At lower pressures, methane adsorption tends to be negatively influenced as the water blocks the pore throats and effective sites. More than just adsorption, water may interact and alter the pores with hydrophilic surface, while Li et al. (2017) did modeling studies to propose that within pores

>2 nm, the critical RH of water desorption is higher than ~20%, so at increased pressures, methane could have a greater chance of transporting and interacting with the altered pores. This explains why the negative moisture effect reduces with increasing pressures at the lowest water content. However, to achieve more realistic adsorption behavior for deep reservoirs, a confining stress should be included, which might lead to different results. At higher confining pressures, the alteration of the pores by water is largely limited. Unfortunately, this alteration cannot be measured in crushed samples that do not experience confining stresses.

For further analysis, the variations in the ALT with the methane and moisture content are presented in Figures 13-15. With the increasing moisture content, the average ALT decreases from 0.60 to 0.43 nm in S_#1, from 0.48 to 0.26 nm in S_#2, and from 0.23 to 0.20 nm in S_#3 at ~9 MPa. ALT reduction exhibits a weaker response to the lowest moisture content. Given the lower limit of pore width accessibility, the small amount of water in ultramicropores is expected to affect methane adsorption slightly. However, increasing adsorbed water impedes the potential well; thus, methane fails to form the same multilayer onto the water-occupied surface (Jin & Firoozabadi, 2014). It is noted that the model may underestimate the result as it is based on an unchanged surface area with weaker interaction in the presence of water (Li et al., 2016). However, with the increasing water content, the water-influenced gas-surface interaction may be so weak that the surfaces are ineffective to methane.

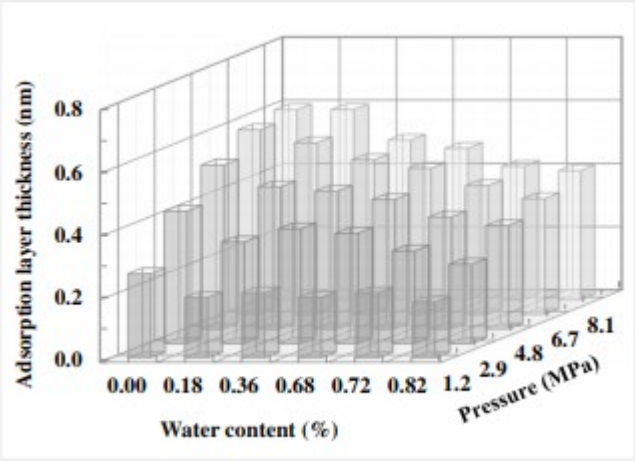

Figure 13

Changes in the adsorbed layer thickness of methane with varying moisture contents and pressures in S_#1.

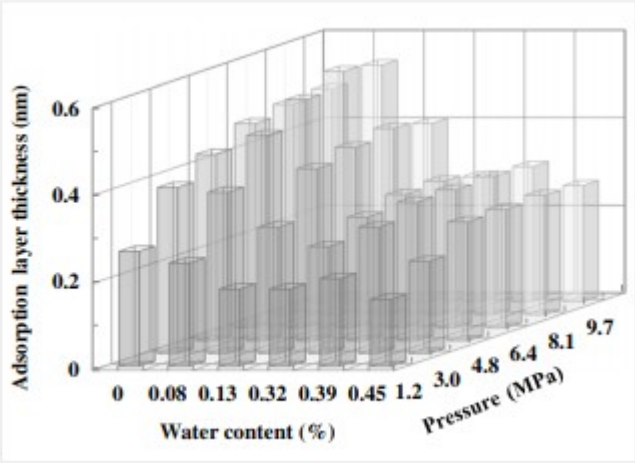

Figure 14

Changes in the adsorbed layer thickness of methane with varying moisture contents and pressures in S_#2.

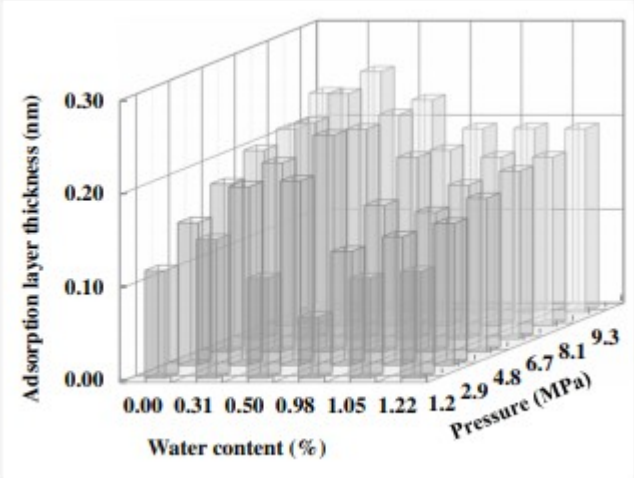

Figure 15

Changes in the adsorbed layer thickness of methane with varying moisture contents and pressures in S_#3.

When the pressure increases from 1 to 9 MPa, increases of the ALT of approximately 0.048, 0.026 and 0.014 nm per pressure unit (1 MPa) are observed in the dry samples of S_#1, S_#2, and S_#3; these values decrease to 0.033, 0.013, and 0.010 nm per pressure unit (1 MPa) in the samples with the highest water content. A higher reduction of the ALT increasing rate is observed in S_#2, in part because of its less accessible path. However, a distinctive increase of water for RH > 75% casts a relatively limited influence on the ALT accumulation of all the samples. In summary, the hydrophilic/hydrophobic characteristics and locations of the effective sites are closely related to the methane behavior under the given moisture conditions, and the ALT clearly changes within a certain moisture

content range, which is 0.18% < ω < 0.68% for S_#1, 0.08% < ω < 0.32% for S_#2, and 0.50% < ω < 0.98% for S_#3.

5 Conclusions

This study investigated the influences of water on methane adsorption in three partially saturated shales. In samples with lower moisture contents, we found that a hint of moisture affects the methane adsorption less, especially at high methane pressures. When the moisture content is increased, moisture clearly impedes methane adsorption. The experimental data indicate that clay-rich shales exhibit a higher resistance to the influence of water. Clays may attract water into their interlayer pores, which limits the formation of obstacles that prevent methane from reaching the adsorption sites. After reaching a specific threshold of water content, additional moisture has little or no impact on methane adsorption in our crushed samples. The methane capacity of the studied shales decreases by 13–42% at the highest moisture content. It is worth noting that the moisture-influenced methane adsorption experiments on bulk shale may lead to different results when the confining stress may limit reshaping of the pores and gas transport.

An optimized model based on the approximation of adsorbed methane density was proposed. The variation of the adsorbed layer thickness suggests that the influence of water–shale interaction on methane behavior is pressure and water content dependent. The hydrophilic/hydrophobic characteristics and locations of the effective sites are closely related to the methane behavior, and the ALT clearly changes within a certain moisture content range.

Acknowledgments

This work was supported in part by China University of Geosciences (Beijing), Beijing, China. The work was funded by the Center for Hydrogeology and Environmental Geology and by the National Natural Sciences Foundation of China (grant 40772208 and 41272387). Financial support from the China Geological Survey program (12120115003301). Work conducted at LBNL was in part supported by the U.S. Department of Energy, Office of Fossil Energy, Office of Natural Gas and Petroleum Technology, through the National Energy Technology Laboratory (NETL), under award DE-AC02-05CH11231 and FWP-ESD14085. The code and data for tables and figures are available online: https://github.com/silverriver/CH4Adsorption.

Appendix A.

Experiments were performed in the presence of a bulk phase to obtain the Gibbs adsorption, which is defined as the total amount of gas present in the two-phase system minus the amount in the gas phase (Sudibandriyo et al., 2003):

$$n_{\text{Gibbs}} = n_{\text{total}} - \rho_{\text{gas}} V_{\text{void}} \quad \text{(A1)}$$

where n_{Gibbs} is the amount of Gibbs adsorption of the gas, n_{total} is the total amount of gas before adsorption, and ρ_{gas} is the bulk gas density. At a planar solid-fluid interface, it is natural to place the dividing surface at the surface of the solid (Myers & Monson, 2002), and most theories of adsorption in porous materials are based on the assumption that adsorption onto the external surface of the solid can be neglected. Numerous authors have assumed that V_{void} remains unchanged with the increasing pressure and have obtained the void volume from helium expansion (Heller & Zoback, 2014; Tan et al., 2014; Weniger et al., 2010; Zhang et al., 2012).

The Gibbs dividing surface approximation yields an accurate isotherm at low pressures but risks potential inaccuracy at high pressures: the adsorption amount is near zero, which makes it more sensitive to ρ_{gas} and the demarcation of the Gibbs dividing surface. On one hand, ρ_{gas} at 314.4 K varies from 6.22 kg/m^3 at 1 MPa to 107.42 kg/m^3 at 15 MPa, which represents a nearly 18-fold difference. Therefore, an underestimated or overestimated V_{void} would inevitably cause larger errors at increased pressures. On the other hand, accessible pores experience saturation at higher pressures, but they are neglected in the Gibbs data processing method. This approach is acceptable in the low-pressure range because most of the pores are available, negligibly influencing the availability of V_{void}. However, at higher pressures, the space for bulk gas, which is expected to decrease, is still represented by the constant V_{void}; thus, the larger term of $V_{void} \times \rho_{gas}$ in equation AA3 will easily cause the adsorption maximum in the high-pressure range.

Although the isotherm was correctly obtained from accurate pressure and temperature monitoring, the Gibbs adsorption isotherm could only describe the difference between the average densities of the fluids inside and outside the effective pores, as a comparative amount that does not give the estimated shale capacity.

Estimating the actual adsorption amount, which is the “absolute adsorption amount,” requires the consideration of the adsorbed phase volume from the boundary where the adsorbed density and bulk density are equal, according to the definition of the Gibbs dividing surface (Do & Do, 2003; Murata & Kaneko, 2000). Existing models give different results depending on their underlying theories and methods, and here, a data processing method without the participation of models is proposed, with the core part being the exclusion of the “inaccessible volume.” The new calculation procedures are given in equations A2 to A6:

$$n_{before} = \frac{P_r}{Z_r R T_r} V_r + \frac{P_s}{Z_s R T_s} V_{void} \quad \text{(A2)}$$

$$V_{void(i)} = V_{void} - \frac{m_{ads}}{\rho_{ads}} \quad \text{(A3)}$$

$$n_{\text{after}} = \frac{P_r'}{Z_r' R T_r'} V_r + \frac{P_s'}{Z_s' R T_s'} V_{\text{void}}' \quad \text{(A4)}$$

$$V_{\text{void}(i)}' = V_{\text{void}}' - \frac{m_{\text{ads}}'}{\rho_{\text{ads}}} \quad \text{(A5)}$$

$$n_{\text{ads}} = \frac{n_{\text{before}} - n_{\text{after}}}{m_s} \quad \text{(A6)}$$

where n_{before} and n_{after} are the total amounts of bulk gas before and after adsorption, respectively; m_{ads} is the mass of the adsorbed gas; a prime (′) denotes the state after adsorption; and (i) (i = 1,2 …) corresponds to the parameter after the ith iteration. In our calculation, the density of liquid methane (ρ_{ads} = 0.421 g/cm^3) was used in equations A3 and A5 (Sudibandriyo et al., 2003), which could provide a lower limit to the added volume at every pressure step. For the first data point, P_s and m_{ads} in equations A2 and A3 were zero because gas had yet to adsorb. m'_{ads} in equation A5 was obtained from n_{ads} in equation A6. Then, $V'_{\text{void(i)'}}$from equation A5 was used to substitute V'_{void} in equation A4 to obtain the new n_{after} and the new n_{Gibbs} from equation A6. For the second data point, m_{ads} in equation A3 was assigned by the new adsorbed gas amount, and the remaining data points were obtained following the same approach. The iteration can be repeated according to the actual situation, and for our experiments, the difference between $V_{\text{void(1)}}$ and $V_{\text{void(2)}}$ was reduced to <0.01 cm^3.

The main goal of this iterative method is to allow the void volumes in equations A2 and A4 to exclude the volume that is saturated by the adsorbed gas, inaccessible to the bulk gas even at elevated pressures. In this way, we could also obtain the updated void volume in every data processing trial. The loss of void volume because of the occupation of methane is due to pressure; it decreases significantly at lower pressures and cumulatively affects the adsorption data processing at higher pressures. The volume loss also increases as the gas adsorption capacity is approached. For instance, the amount of methane adsorption can reach 1.2 mmol/g in coal (Zhang et al., 2012), which is nearly 20 times greater than that of our sample. Ignoring the volume loss leads to a significant underestimation of the adsorption amount.

References

Ambrose, R. J., Hartman, R. C., Diaz Campos, M., Akkutlu, I. Y., & Sondergeld, C. (2010). *New pore-scale considerations for shale gas in place calculations*. Paper presented at SPE Unconventional Gas Conference, Society of Petroleum Engineers, Pittsburgh, PA. https://doi.org/10.2118/131772-MS

Busch, A., Gensterblum, Y., Krooss, B. M., & Littke, R. (2004). Methane and carbon dioxide adsorption–diffusion experiments on coal: Upscaling and

modeling. *International Journal of Coal Geology*, 60(2–4), 151– 168. https://doi.org/10.1016/j.coal.2004.05.002

Chalmers, G. R. L., & Bustin, R. M. (2008). Lower Cretaceous gas shales in northeastern British Columbia. Part I: Geological controls on methane sorption capacity. *Bulletin of Canadian Petroleum Geology*, 56(1), 1– 21. https://doi.org/10.2113/gscpgbull.56.1.1

Chen, S., Zhu, Y., Wang, H., Liu, H., Wei, W., & Fang, J. (2011). Shale gas reservoir characterisation: A typical case in the southern Sichuan basin of China. *Energy*, 36(11), 6609– 6616. https://doi.org/10.1016/j.energy.2011.09.001

Chenevert, M. E. (1970). Shale alteration by water adsorption. *Journal of Petroleum Technology*, 22(09), 1141– 1148. https://doi.org/10.2118/2401-PA

Clarkson, C. R., & Bustin, R. M. (2000). Binary gas adsorption/desorption isotherms: Effect of moisture and coal composition upon carbon dioxide selectivity over methane. *International Journal of Coal Geology*, 42(4), 241– 271. https://doi.org/10.1016/S0166-5162(99)00032-4

Coleman, T. F., & Li, Y. (1996). A reflective newton method for minimizing a quadratic function subject to bounds on some of the variables. *SIAM Journal on Optimization*, 6(4), 1040– 1058. https://doi.org/10.1137/S1052623494240456

Crosdale, P. J., Moore, T. A., & Mares, T. E. (2008). Influence of moisture content and temperature on methane adsorption isotherm analysis for coals from a low-rank, biogenically-sourced gas reservoir. *International Journal of Coal Geology*, 76(1-2), 166– 174. https://doi.org/10.1016/j.coal.2008.04.004

Do, D. D., & Do, H. D. (2003). Adsorption of supercritical fluids in non-porous and porous carbons: Analysis of adsorbed phase volume and density. *Carbon*, 41(9), 1777– 1791. https://doi.org/10.1016/S0008-6223(03)00152-0

Fitzgerald, J. E., Pan, Z., Sudibandriyo, M., Robinson, R. L. Jr., Gasem, K. A. M., & Reeves, S. (2005). Adsorption of methane, nitrogen, carbon dioxide and their mixtures on wet Tiffany coal. *Fuel*, 84(18), 2351– 2363. https://doi.org/10.1016/j.fuel.2005.05.002

Greenspan, L. (1977). Humidity fixed points of binary saturated aqueous solutions. *Journal of Research of the National Bureau of Standards Section A: Physics and Chemistry*, 81A(1), 81– 89. https://doi.org/10.6028/jres.081A.011

Groen, J. C., Peffer, L. A. A., & Pérez-Ramírez, J. (2003). Pore size determination in modified micro- and mesoporous materials. Pitfalls and limitations in gas adsorption data analysis. *Microporous and Mesoporous Materials*, 60(1–3), 1– 17. https://doi.org/10.1016/S1387-1811(03)00339–1

Guo, H., Jia, W., Peng, P., Lei, Y., Luo, X., Cheng, M., et al. (2014). The composition and its impact on the methane sorption of lacustrine shales from the Upper Triassic Yanchang formation, Ordos basin, China. *Marine and Petroleum Geology*, 57(2), 509– 520. https://doi.org/10.1016/j.marpetgeo.2014.05.010

Hartman, R. C., Lasswell, P., & Bhatta, N. (2008). *Recent advances in the analytical methods used for shale gas reservoir gas-in-place assessment*. San Antonio, Texas: AAPG Annual Convention. April 20–23

Hatch, C. D., Wiese, J. S., Crane, C. C., Harris, K. J., Kloss, H. G., & Baltrusaitis, J. (2012). Water adsorption on clay minerals as a function of relative humidity: Application of BET and Freundlich adsorption models. *Langmuir: The ACS Journal of Surfaces and Colloids*, 28(3), 1790– 1803. https://doi.org/10.1021/la2042873

Heller, R., & Zoback, M. (2014). Adsorption of methane and carbon dioxide on gas shale and pure mineral samples. *Journal of Unconventional Oil and Gas Resources*, 8, 14– 24. https://doi.org/10.1016/j.juogr.2014.06.001

Ji, L., Zhang, T., Milliken, K. L., Qu, J., & Zhang, X. (2012). Experimental investigation of main controls to methane adsorption in clay-rich rocks. *Applied Geochemistry*, 27(12), 2533– 2545. https://doi.org/10.1016/j.apgeochem.2012.08.027

Jin, Z., & Firoozabadi, A. (2014). Effect of water on methane and carbon dioxide sorption in clay minerals by Monte Carlo simulations. *Fluid Phase Equilibria*, 382, 10– 20. https://doi.org/10.1016/j.fluid.2014.07.035

Joubert, J. I., Grein, C. T., & Bienstock, D. (1974). Effect of moisture on the methane capacity of American coals. *Fuel*, 53(3), 186– 191. https://doi.org/10.1016/0016-2361(74)90009-X

Kang, S. M., Fathi, E., Ambrose, R. J., Akkutlu, I. Y., & Sigal, R. F. (2011). Carbon dioxide storage capacity of organic-rich shales. *SPE Journal*, 16(04), 842– 855. https://doi.org/10.2118/134583-PA

Kowalczyk, P., Tanaka, H., Kaneko, K., Terzyk, A. P., & Do, D. D. (2005). Grand canonical Monte Carlo simulation study of methane adsorption at an open graphite surface and in slit-like carbon pores at 273 K. *Langmuir: The ACS Journal of Surfaces and Colloids*, 21(12), 5639– 5646. https://doi.org/10.1021/la050126f

Krooss, B. M., Van Bergen, F., Gensterblum, Y., Siemons, N., Pagnier, H. J. M., & David, P. (2002). High-pressure methane and carbon dioxide adsorption on dry and moisture-equilibrated Pennsylvanian coals. *International Journal of Coal Geology*, 51(2), 69– 92. https://doi.org/10.1016/S0166-5162(02)00078-2

Levy, J. H., Day, S. J., & Killingley, J. S.a. (1997). Methane capacities of Bowen Basin coals related to coal

properties. *Fuel*, 76(9), 813– 819. https://doi.org/10.1016/S0016-2361(97)00078-1

Li, J., Li, X., Wang, X., Li, Y., Wu, K., Shi, J., et al. (2016). Water distribution characteristic and effect on methane adsorption capacity in shale clay. *International Journal of Coal Geology*, 159, 135– 154. https://doi.org/10.1016/j.coal.2016.03.012

Li, J., Li, X., Wu, K., Feng, D., Zhang, T., & Zhang, Y. (2017). Thickness and stability of water film confined inside nanoslits and nanocapillaries of shale and clay. *International Journal of Coal Geology*, 179, 253– 268. https://doi.org/10.1016/j.coal.2017.06.008

Li, Y., Li, X., Wang, Y., & Yu, Q. (2015). Effects of composition and pore structure on the reservoir gas capacity of Carboniferous shale from Qaidam Basin, China. *Marine and Petroleum Geology*, 62, 44– 57. https://doi.org/10.1016/j.marpetgeo.2015.01.011

Liu, Y., Zhu, Y., Li, W., Xiang, J., Wang, Y., Li, J., & Zeng, F. (2016). Molecular simulation of methane adsorption in shale based on grand canonical Monte Carlo method and pore size distribution. *Journal of Natural Gas Science and Engineering*, 30, 119– 126. https://doi.org/10.1016/j.jngse.2016.01.046

Merkel, A., Fink, R., & Littke, R. (2015). The role of pre-adsorbed water on methane sorption capacity of Bossier and Haynesville shales. *International Journal of Coal Geology*, 147–148, 1– 8. https://doi.org/10.1016/j.coal.2015.06.003

Merkel, A., Gensterblum, Y., Krooss, B. M., & Amann, A. (2015). Competitive sorption of CH_4, CO_2 and H_2O on natural coals of different rank. *International Journal of Coal Geology*, 150–151, 181– 192. https://doi.org/10.1016/j.coal.2015.09.006

Mosher, K., He, J., Liu, Y., Rupp, E., & Wilcox, J. (2013). Molecular simulation of methane adsorption in micro- and mesoporous carbons with applications to coal and gas shale systems. *International Journal of Coal Geology*, 109–110, 36– 44. https://doi.org/10.1016/j.coal.2013.01.001

Murata, K., & Kaneko, K. (2000). Nano-range interfacial layer upon high-pressure adsorption of supercritical gases. *Chemical Physics Letters*, 321(5–6), 342– 348. https://doi.org/10.1016/S0009-2614(00)00367-5

Myers, A. L., & Monson, P. A. (2002). Adsorption in porous materials at high pressure: Theory and experiment. *Langmuir*, 18(26), 10,261– 10,273. https://doi.org/10.1021/la026399h

Rexer, T. F., Mathia, E. J., Aplin, A. C., & Thomas, K. M. (2014). High-pressure methane adsorption and characterization of pores in Posidonia shales and isolated kerogens. *Energy and Fuels*, 28(5), 2886– 2901. https://doi.org/10.1021/ef402466m

Ross, D. J. K., & Bustin, R. M. (2007a). Impact of mass balance calculations on adsorption capacities in microporous shale gas reservoirs. *Fuel*, 86(17–18), 2696– 2706. https://doi.org/10.1016/j.fuel.2007.02.036

Ross, D. J. K., & Bustin, R. M. (2007b). Shale gas potential of the Lower Jurassic gordondale member, northeastern British Columbia, Canada. *Bulletin of Canadian Petroleum Geology*, 55(1), 51– 75. https://doi.org/10.2113/gscpgbull.55.1.51

Sudibandriyo, M., Pan, Z., Fitzgerald, J. E., Robinson, R. L., & Gasem, K. A. M. (2003). Adsorption of methane, nitrogen, carbon dioxide, and their binary mixtures on dry activated carbon at 318.2 K and pressures up to 13.6 MPa. *Langmuir*, 19(13), 5323– 5331. https://doi.org/10.1021/la020976k

Tan, J., Weniger, P., Krooss, B., Merkel, A., Horsfield, B., & Zhang, J. (2014). Shale gas potential of the major marine shale formations in the Upper Yangtze Platform, South China. Part II: Methane sorption capacity. *Fuel*, 129, 204– 218. https://doi.org/10.1016/j.fuel.2014.03.064

Titiloye, J. O., & Skipper, N. T. (2000). Computer simulation of the structure and dynamics of methane in hydrated Na-smectite clay. *Chemical Physics Letters*, 329(1–2), 23– 28. https://doi.org/10.1016/S0009-2614(00)00975-1

Tokunaga, T. K., Shen, W., Wan, J., Kim, Y., Cihan, A., Zhang, Y., & Finsterle, S. (2017). Water saturation relations and their diffusion-limited equilibration in gas shale: Implications for gas flow in unconventional reservoirs. *Water Resources Research*, 53, 9757– 9770. https://doi.org/10.1002/2017WR021153

Wang, L., & Yu, Q. (2016). The effect of moisture on the methane adsorption capacity of shales: A study case in the eastern Qaidam basin in China. *Journal of Hydrology*, 542, 487– 505. https://doi.org/10.1016/j.jhydrol.2016.09.018

Weniger, P., Kalkreuth, W., Busch, A., & Krooss, B. M. (2010). High-pressure methane and carbon dioxide sorption on coal and shale samples from the Paraná Basin, Brazil. *International Journal of Coal Geology*, 84(3–4), 190– 205. https://doi.org/10.1016/j.coal.2010.08.003

Yang, K., Lu, X., Lin, Y., & Neimark, A. V. (2010). Deformation of coal induced by methane adsorption at geological conditions. *Energy and Fuels*, 24(11), 5955– 5964. https://doi.org/10.1021/ef100769x

Yee, D., Seidle, J. P., & Hanson, W. B. (1993). Gas sorption on coal and measurement of gas. In B. E. Law & D. D. Rice (Eds.), *Gas Sorption on Coal and Measurement of Gas, in Hydrocarbons From Coal. AAPG/Datapages* (pp. 203– 218). Tulsa, OK: American Association of Petroleum Geologists.

Yuan, W., Pan, Z., Li, X., Yang, Y., Zhao, C., Connell, L. D., et al. (2014). Experimental study and modelling of methane adsorption and

diffusion in
shale. *Fuel*, 117, 509– 519. https://doi.org/10.1016/j.fuel.2013.09.046

Zhang, T., Ellis, G. S., Ruppel, S. C., Milliken, K., & Yang, R. (2012). Effect of organic-matter type and thermal maturity on methane adsorption in shale-gas systems. *Organic
Geochemistry*, 47, 120– 131. https://doi.org/10.1016/j.orggeochem.2012.03.012

Zhang, T., Yang, R., Milliken, K. L., Ruppel, S. C., Pottorf, R. J., & Sun, X. (2014). Chemical and isotopic composition of gases released by crush methods from organic rich mudrocks. *Organic
Geochemistry*, 73(3), 16– 28. https://doi.org/10.1016/j.orggeochem.2014.05.003

Zheng, Y., & Gu, T. (1998). Modified van der Waals equation for the prediction of multicomponent isotherms. *Journal of Colloid and Interface Science*, 206(2), 457– 463. https://doi.org/10.1006/jcis.1998.5733

Zhou, L., Zhou, Y., Li, M., Chen, P., & Wang, Y. (2000). Experimental and modeling study of the adsorption of supercritical methane on a high surface activated
carbon. *Langmuir*, 16(14), 5955– 5959. https://doi.org/10.1021/la991159w